

Ultra-Stable, Endurable, and Flexible $Sb_2Te_xSe_{3-x}$ Phase Change Devices for Memory Application and Wearable Electronics

Shubing Li, Ming Li, Li Chen, Xionghu Xu, Anyang Cui,* Xin Zhou, Kai Jiang, Liyan Shang, Yawei Li, Jinzhong Zhang, Liangqing Zhu, Zhigao Hu,* and Junhao Chu



Cite This: *ACS Appl. Mater. Interfaces* 2022, 14, 45600–45610



Read Online

ACCESS |

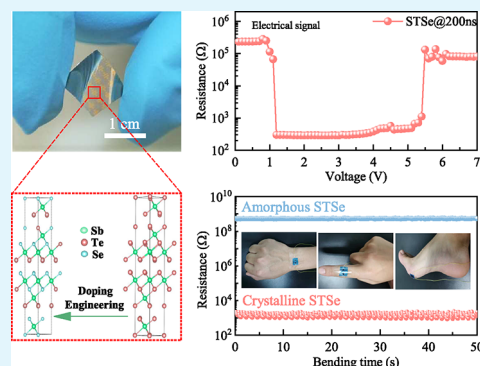
Metrics & More

Article Recommendations

Supporting Information

ABSTRACT: Flexible memory and wearable electronics represent an emerging technology, thanks to their reliability, compatibility, and superior performance. Here, an $Sb_2Te_xSe_{3-x}$ (STSe) phase change material was grown on flexible mica, which not only exhibited superior nature in thermal stability for phase change memory application but also revealed novel function performance in wearable electronics, thanks to its excellent mechanical reliability and endurance. The thermal stability of Sb_2Te_3 was improved obviously with the crystallization temperature elevated 60 K after Se doping, for the enhanced charge localization and stronger bonding energy, which was validated by the Vienna *ab initio* simulation package calculations. Based on the ultra-stability of STSe, the STSe-based phase change memory shows 65 000 reversible phase change ability. Moreover, the assembled flexible device can show real-time monitoring and recoverability response in sensing human activities in different parts of the body, which proves its effective reusability and potential as wearable electronics. Most importantly, the STSe device presents remarkable working reliability, reflected by excellent endurance over 100 s and long retention over 100 h. These results paved a novel way to utilize STSe phase change materials for flexible memory and wearable electronics with extreme thermal and mechanical stability and brilliant performance.

KEYWORDS: $Sb_2Te_xSe_{3-x}$ phase change materials, ultra-stability, phase change memory, wearable electronics



These results paved a novel way to utilize STSe phase change materials for flexible memory and wearable electronics with extreme thermal and mechanical stability and brilliant performance.

1. INTRODUCTION

With the rapid development of information technology, the growing demand for data storage has increased exponentially in recent decades.¹ Non-volatile memories for high-density data storage and neuro-inspired computing are promising technologies to cope with the burden.² Among the several emerging memory technologies, phase change random access memory (PCRAM) is a mature and leading candidate for next-generation electronic devices, thanks to its high operation speed, low scaling limit, and great compatibility with the standard complementary metal oxide semiconductor technology.^{3–8} Zhu and Song *et al.* have provided a much increased storage density by presenting a single-element electrical switch and utilizing reversible multi-level phase transitions.⁹ The mechanism of PCRAM relies on the phase change material (PCM) to store “0” or “1” by the reversible structural transition between the crystalline state (low-resistance state, LRS) and amorphous state (high-resistance state, HRS). Moreover, a PCRAM chip exhibits good reliability under the circumstances of sub-20 nm technology with below $4F^2$ cell size.¹⁰ In practice, PCRAM is usually applied to rigid substrates such as silicon,^{11,12} sapphire, and quartz,¹³ while little work uses the flexible substrate.

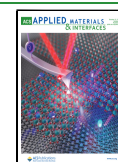
In the last several years, flexible PCRAM has been widely perceived as a feasible solution for advanced data storage devices due to its excellent electrical properties, reliability, and power efficiency.^{14–17} Meanwhile, flexible electronics are being developed at a tremendous pace and routinely used on many occasions, featured by superior bending stability, portability, compatibility, and light weight. However, the mechanical deformation is inevitable in flexible devices, such as compression, tension, and twist, which is unfriendly to the performance and properties of the flexible electronics. In addition, the favorable data retention at high temperature is also necessary, such as an automotive system.¹⁸ Therefore, as one of the most important steps in fabricating PCRAM, it is necessary to search for a reliable PCM to enable thermal and mechanical ultra-stability and benign performance.

As a typical PCM, Sb_2Te_3 (ST) is one of the elements on the ST–GeTe pseudo-binary system that constitutes $Ge_2Sb_2Te_3$

Received: August 1, 2022

Accepted: September 19, 2022

Published: September 30, 2022



(GST) and exhibits a good prospect for PCRAM application owing to its faster operation speed than that of GST. As a grain growth-domain PCM, ST possesses high crystallization speed, and subnanosecond SET (amorphous state to crystalline state) speeds could be achieved by Sc-doped ST-based PCRAM.¹⁹ Nevertheless, the low crystallization temperature and unsatisfied thermal stability from the amorphous state of ST limited the application in phase change memory.

As a simple and effective method, doping engineering is employed to achieve high stability for ST, in which various dopants such as Sc,¹⁹ Er,²⁰ Ge,²¹ N,²² Ti,^{23–25} Y,²⁶ and Ag–In²⁷ have been attempted and investigated, and the role of the dopant can be determined with the help of atomic-scale micrology and simulations.^{20,27} However, most of the studies have focused on the cation substitution by replacing Sb, while only a few studies pay attention to anion substitution.^{28,29} Anion substitution of Te for Se can increase the band gap.³⁰ Thus, the resistance and the thermal stability of $\text{Sb}_2\text{Te}_x\text{Se}_{3-x}$ (STSe) could be elevated. In addition, Se can be utilized to improve the crystallization temperature of Sb_4Te and overcome the thermal stability limit of GeTe for high-temperature applications, with phase change temperature elevated more than 100 K after proper Se content doping.^{31,32} Beyond this, Se-based PCMs, such as $\text{Ge}_2\text{Sb}_2\text{Se}_4\text{Te}_1$ and Sb_2Se_3 , show a good application prospect in the field of reconfigurable non-volatile metasurfaces^{30,33–35} and low-loss waveguide transmission in photonic integrated circuits.³⁶ Moreover, Se has higher electronegativity than Te due to its stronger metalloid character, indicating the stronger interaction between Sb and Se than that between Sb and Te accompanied with stable mechanical properties. Inspired by this feature, flexible STSe may provide a novel function performance to realize stable and enduring devices and wearable electronics, such as human activity sensing. Therefore, STSe films are expected to solve the dilemma between lower thermal stability and faster crystallization speed in the Sb–Te alloys and demonstrate satisfied thermal and mechanical stability with decent electrical properties for developing flexible PCRAM and wearable electronic applications.

In this work, the bendable ST and STSe device elements were deposited on a flexible mica sheet, and the mechanism of Se incorporation into ST was investigated systematically. The incorporation of Se not only increased the phase change temperature and thermal stability of ST but also improved the mechanical stability. Profiting from the large resistance contrast and benign recoverability response, the assembled STSe flexible devices exhibited a superior performance in sensing human activities. Moreover, up to a 10^6 ON/OFF ratio and long-term operating reliability can be well kept up after mechanical fatigue dynamic bending for 100 s and static bending for 100 h, which can be ascribed to the enhanced localization and stronger Sb–Se bonds than Sb–Te bonds according to charge density difference (CDD) simulation. The obtained results may open up a new route to utilize STSe PCMs for flexible PCRAM application and high-performance wearable electronics.

2. EXPERIMENTAL SECTION

2.1. Film Deposition. First, all the used substrates were cleaned using a standard process, using detergent, acetone, and ethanol in succession. Then, ST and STSe films were deposited based on the pulsed laser deposition (PLD) technique. A KrF excimer laser beam with a wavelength of 248 nm and a pulse length of 20 ns was

employed. The background pressure in the PLD chamber was 7.0×10^{-7} mbar. During deposition, highly pure argon was used, resulting in a pressure of 1.0×10^{-2} mbar. To obtain a clean surface, the substrates were cleaned using detergent, acetone, and ethanol in succession. The cleaned substrates were positioned inside the chamber at a distance between the target and substrate of 5.5 cm. Commercial ST and STSe targets were utilized and rotated continuously in order to improve the uniformity of the phase change films. Moreover, in an attempt to acquire crystalline ST and STSe samples, the as-deposited films were annealed at the corresponding temperature in an argon atmosphere to prevent oxidation.

2.2. Fabrication of Devices. For achieving a vertical sandwich structure during phase change memory fabrication, the back electrodes were patterned by electron beam lithography (EBL) first. The W micro-heater (100 nm, $50 \mu\text{m} \times 100 \mu\text{m}$) electrodes were deposited by magnetron sputtering, followed by the lift-off process. Then, the PCM layers were deposited by aforementioned PLD (~ 70 nm, $3.5 \mu\text{m} \times 4.5 \mu\text{m}$). Furthermore, the Ni/Au (2/60 nm, $50 \mu\text{m} \times 100 \mu\text{m}$) top electrodes were sputtered. Finally, the 100 nm-thick dense-sputtered SiO_2 capping layer was used to improve the device stability and cyclicity in the operation process. All layers of the vertical sandwich structure phase change memory were patterned by EBL. The detailed fabrication process flow and size of each device can be seen in Figures S1 and 6b, respectively.

For fabricating wearable electronics, the mica substrates were selected, thanks to their high flexibility and decent thermal resistance, and mechanically exfoliated to $\sim 20 \mu\text{m}$ from the fluorophlogopite mica crystal [$\text{KMg}_3(\text{AlSi}_3\text{O}_{10})\text{F}_2$] to realize high suppleness. The 100 nm-thick ST and STSe layers were deposited by PLD. For electrical measurement, the Ni/Au top electrode was evaporated using a thermal evaporation machine through a shadow mask. The active area of each isolated device was 0.04 mm^2 , which can be modified and defined by the size of the shadow mask.

2.3. Characterizations. The structural characteristics of ST and STSe thin films were measured by X-ray diffraction (XRD, Japan SmartLab) with Cu $K\alpha$ radiation from 5 to 60° and a scanning rate of $0.02^\circ/\text{s}$. The surface morphology of the samples was studied by atomic force microscopy (AFM, Dimension Icon, Bruker). The chemical valence and chemical composition were acquired by X-ray photoelectron spectroscopy (XPS, Thermo ESCALAB 250Xi) equipped with an Al $K\alpha$ X-ray source, and the spectra were referenced to C 1s at 284.8 eV. In addition, Raman spectroscopy (Jobin-Yvon LabRAM HR Evolution spectrometer) measurements were performed using a 532 nm laser in the range of $50\text{--}300 \text{ cm}^{-1}$ and a THMSE 600 heating/cooling stage (Linkam Scientific Instruments). Besides, the transmittance of the films was recorded using a double-beam UV–vis–NIR spectrophotometer (PerkinElmer Lambda 950). The bending electrical performances and durability of flexible STSe devices were measured at room temperature in a probe station equipped with a semiconductor parameter analyzer (4200-SCS, Keithley). In addition, the temperature-dependent electrical properties were measured by utilizing the electrical measuring stage, which consisted of a Keithley 2400 SourceMeter and a THMSE 600 heating/cooling stage. The scanning transmission electron microscopy (STEM) specimen was prepared with a dual-beam focused ion beam system (Nanolab Helios 650). The high-resolution transmission electron microscopy (HRTEM) images and energy-dispersive X-ray spectroscopy (EDS) elemental mapping were captured using the STEM mode of JEM Grand ARM300F with a probe corrector and an EDS detector operated at 300 kV.

2.4. DFT Simulations. The computational calculations were implemented using the framework of density functional theory (DFT) based on the Vienna *ab initio* simulation package. The generalized gradient approximation of Perdew–Burke–Ernzerhof potential is used. The γ point was used to sample the Brillouin zone of the supercell. In the calculations, the kinetic energy cutoff plane wave was set to 300 eV for the plane-wave expansion of wave functions with an energy accuracy of 10^{-8} eV. The maximum residual force was less than $0.001 \text{ eV } \text{\AA}^{-1}$. In addition, the valence electron configurations for Sb, Te, and Se were $5s^25p^3$, $5s^25p^4$, and $4s^24p^4$, respectively. For

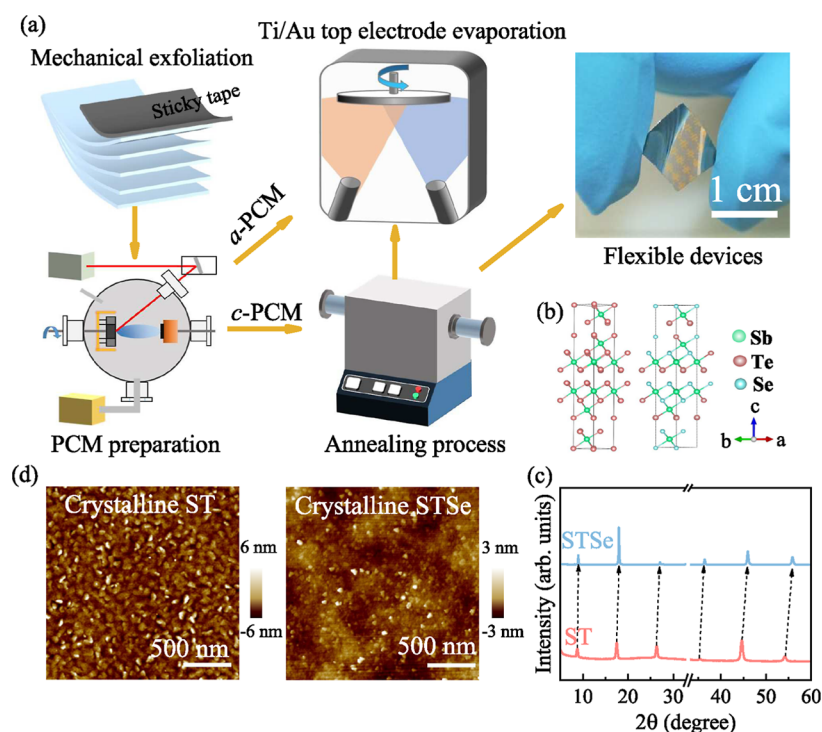


Figure 1. (a) Schematic diagram of mica/PCM/top electrode flexible device preparation. (b) Schematic of ST and STSe crystal structures. (c) XRD patterns of the crystalline ST and STSe films. (d) AFM images of the crystalline ST and STSe films.

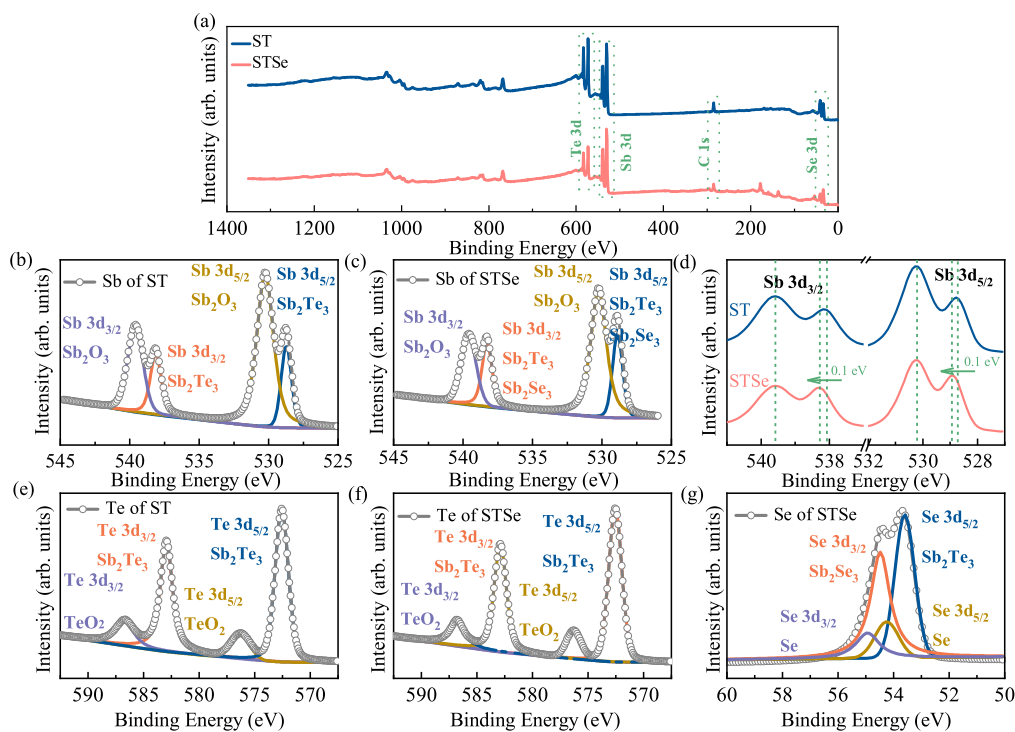


Figure 2. (a) Overall XPS spectra of crystalline ST and STSe films. The fitted XPS spectra of (b) Sb 3d in the ST and (c) Sb 3d in the STSe films. (d) Zoomed-in image of Sb 3d in ST and STSe. The incorporation of Se into ST leads to an increase in the bonding energy of Sb 3d_{3/2}. The fitted XPS spectra of (e) Sb 3d, (f) Te 3d, and (g) Se 3d for the STSe films.

amorphous processes, the typical *NVT* (constant number, volume, and temperature) ensemble was employed based on *ab initio* molecular dynamics simulations. In the amorphous model, a 135-atom (54 Sb and 81 Te) cubic cell of ST and a 135-atom (54 Sb, 35 Te, and 46 Se) cubic cell of STSe were simulated with a periodic boundary condition by canonical *NVT* (constant number, volume,

and temperature) molecular dynamics.^{19,25} The atomic ratios of ST and STSe are modeled with their experimentally derived molecular formula results, Sb₂Te₃ and Sb₂Te_{1.3}Se_{1.7}, respectively. To prepare the amorphous model, the ensemble of atoms was melted and equilibrated at 3000 K for 9 ps and quenched to 1000 K for another 30 ps subsequently and finally cooled down and equilibrated rapidly at

300 K with a quenching rate of -15 K/ps, maintained for another 15 ps.³⁷

3. RESULTS AND DISCUSSION

Figure 1a illustrates the schematic of the PCMs and device preparation process. To better visualize the position of Se atoms in STSe, the crystal structure diagram of ST and STSe in the hexagonal supercell is shown in Figure 1b. Each unit cell of ST contains quintuple layers along the c -axis in the order of Te1–Sb–Te2–Sb–Te1. Moreover, the structural evolution of ST and STSe was investigated by XRD, as shown in Figures 1c and S2. The diffraction peaks of STSe shift to a high angle, as compared with standard ST peaks.^{38–40} Based on the Bragg equation, it can be shown that the increase in diffraction angles was triggered by the decrease in interplanar spacing. From the perspective of the ionic radius of Sb^{3+} (0.76 Å), Te^{2-} (2.21 Å), and Se^{2-} (1.98 Å), we conjecture that the doped Se atoms prefer to occupy the position of Te atoms. Moreover, according to XRD results and the Scherrer formula, the average grain sizes of ST and STSe were calculated to be about 19 and 10.2 nm, respectively, which was in good agreement with the HRTEM and AFM images, as illustrated in Figures S3 and S6, respectively.

In order to reveal the chemical composition and bonding effect of Se doping on ST films, the XPS spectra were implemented and are shown in Figure 2. Figure 2a exhibits the overall XPS spectra of ST and STSe films, in which no peaks of other elements were found except oxygen suggesting the high purity of the film. As shown in Figure 2b, four peaks of Sb of ST are located at 539.6, 538.1, 530.2, and 528.7 eV. The binding energies of 539.6 and 530.2 eV are related to the Sb–O bond of Sb_2O_3 , which can be attributed to the slight surface oxidation common in PCMs,^{30,41} while the doublet peaks at 538.1 and 528.7 eV are attributed to the Sb–Te bond. In addition, the peak positions of Sb_2O_3 for ST and STSe (Figure 2c) almost show no change, indicating that the chemical environment of Sb–O remains the same. However, compared with that of pure ST, the binding energy of electrons associated with the Sb–Te bond after Se doping undergoes a blue shift of 0.1 eV as shown in Figure 2d. It indicates that the increasing order of Sb–Se bond formation is energetically more favored than that of the Sb–Te bond⁴² since Sb possesses large affinity toward Se due to its higher electronegativity (2.55) than that of Te (2.1).⁴³ From the XPS results, it can be concluded that the doped Se atoms occupy the position of Te atoms binding with Sb, which is consistent with the above-mentioned XRD results. As shown in Figure 2e,f, the Te 3d peaks of the Sb–Te bond and Te–O bond are marked at 572.6, 582.9, 576.3, and 586.8 eV.^{26,41} As seen from Figure 2g, the selenium 3d_{5/2} and selenium 3d_{3/2} peaks appeared at 53.6 and 54.5 eV, respectively, which were in accordance with early reports.³⁰ The atomic percentage of Sb/Te was acquired by calculation to be 41.2:58.8 for ST, while the stoichiometric percentage of Sb/Te/Se was calculated to be 40.4:26.3:33.3 for STSe. Moreover, the composition of the STSe target film is virtually unanimous as that of the target, as shown in Table S1 and Figure S4, which is one of the primary advantages of the PLD.⁴¹ As a result, the corresponding molecular formula is Sb_2Te_3 and $\text{Sb}_2\text{Te}_{1.3}\text{Se}_{1.7}$, respectively.

To further understand the bonding properties of ST and STSe, the difference between the self-consistent charge and a superposition of the atomic charge (CDD) isosurface was used to identify areas of electric cloud distribution, which is a key

element to evaluate the charge distribution resulting from the chemical bonding with surrounding atoms. The calculation is based on a superposition of isolated Sb, Te, and Se atoms, which are rendered as green, red, and blue spheres, respectively, as shown in Figure 3. Figure 3a,b presents the

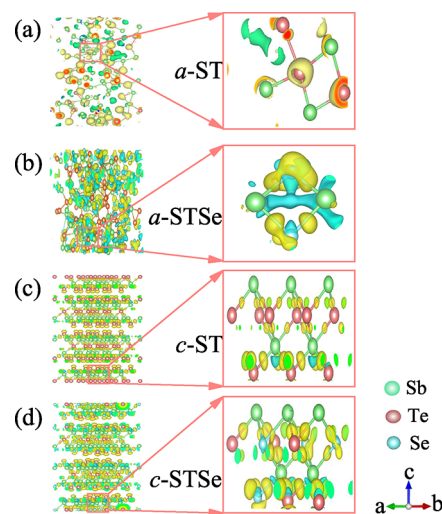


Figure 3. CDD of (a) a-ST, (b) a-STSe, (c) c-ST, and (d) c-STSe. The isosurface value was fixed at $+0.006 e/a_0^3$. The light-yellow and blue isosurfaces represent the positive and negative localized wave functions, respectively. The CDD in ST and STSe clearly depends on the doping of Se.

typical configurations of a-ST and a-STSe as obtained from the melting quench process; as can be seen, all the atoms are randomly distributed in the supercell. In contrast with a-ST, large electron localization and strong electronic cloud density can be clearly visualized at Sb atoms in a-STSe, which is denoted lone-pair electrons or nonbonding electrons.^{37,44} The main reason contributing to the improved stability of a-STSe, compared to that of pristine ST, is the stronger reciprocity between Sb and Se than that between Sb and Te. Figure 3c shows a typical local defective structure pattern for charge localization of c-ST with the electrons accumulated between Sb atoms and Te atoms, which indicates that Sb and Te atoms are covalently bonded.⁴⁵ Compared with pristine c-ST, c-STSe possesses a larger electron clustered at the Sb–Se bonds (Figure 3d), indicating the enhanced localization and stronger Sb–Se bonds than Sb–Te bonds, which is reasonable for the stability of Sb–Se bonds and consistent with XPS results. On the other hand, the unsatisfied thermal stability of amorphous ST constrained the application in phase change memory; consequently, the effect of Se on the thermal stability of a-ST is a major concern for the industry. Furthermore, the CDD always serves as an effective tool to measure bond strength. From the partially enlarged detail, it can be clearly seen that Se holds significantly more charge in its bonds with Sb than Te does, which plays a positive role in the enhanced bond strength. Evidently, the detailed abovementioned analysis of the charge density variation suggesting the structure stability of ST can be significantly enhanced by Se incorporation.

To inspect the structural evolution and the crystallization temperature of ST and STSe films during the phase transition, Raman spectra were plotted separately, as shown in Figure 4. The observed Raman spectra of the ST and STSe films at room temperature show no peak related to the characteristic

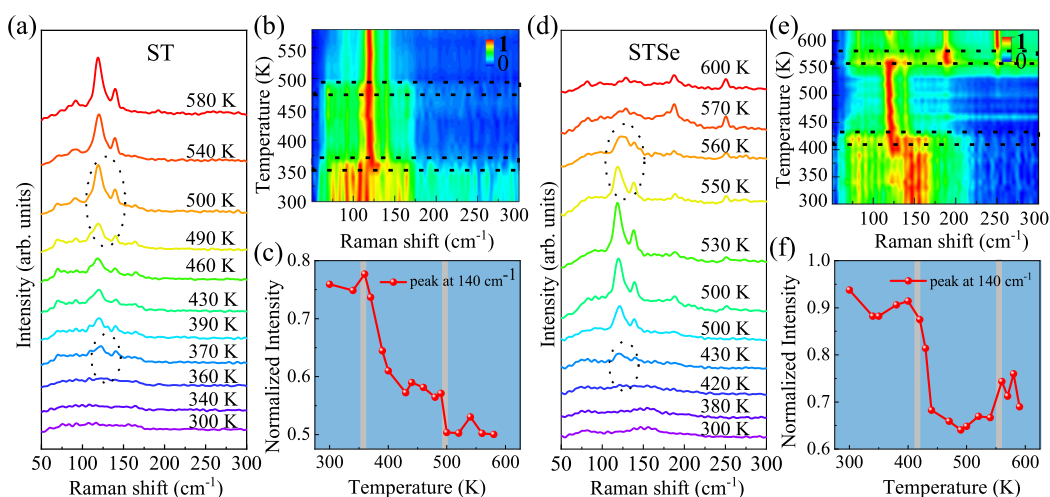


Figure 4. Temperature dependence of Raman scattering spectra for amorphous (a) ST and (d) STSe films with a heating rate of 10 K/min. An intensity-normalized contour map derived from the data in temperature-dependent Raman spectra for the (b) ST and (e) STSe films. Normalized intensity of the peak at 140 cm^{-1} as a function of temperature for (c) ST and (f) STSe.

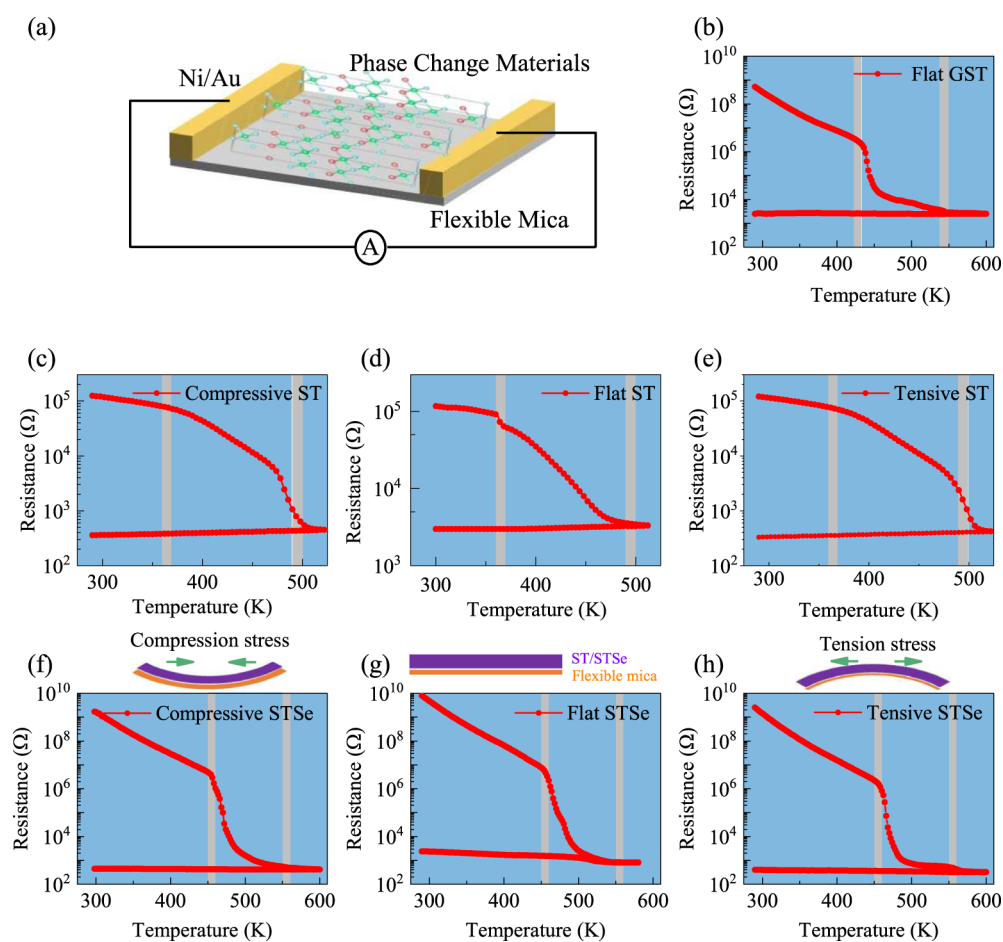


Figure 5. (a) Schematic diagram of temperature-dependent resistance measurement devices. Temperature dependence of the resistance of (b) flat GST, (c) compressive ST, (d) flat ST, (e) tensile ST, (f) compressive STSe, (g) flat STSe, and (h) tensile STSe films at the same heating rate of 10 K/min.

vibrational mode. For undoped ST in Figure 4a, two broad bands centered at 119 and 140 cm^{-1} representing the E_g^2 and A_{2u}^3 modes, respectively,⁴⁶ start occurrence at 370 K with the increasing temperature, suggesting that the ST phase change films crystallize from the amorphous to metastable face-centered cubic (FCC) states. As the temperature increases

further, the Raman spectra of these two vibrational modes exhibit negligible difference. However, the peak at about 119 cm^{-1} suddenly sharpens with further increasing annealing temperature to 500 K , demonstrating the appearance of the hexagonal (HEX) phase.⁴⁷ In order to show the peak intensity change more vividly, the intensity was normalized with the

contour map shown in Figure 4b. The relative intensity shift presents a significant change at 370 and 500 K, which shows that the PCM crystallizes from the amorphous to metastable FCC and ulteriorly transforms into the HEX phase. Meanwhile, the variations can also be observed in Figure 4c. In comparison with that of ST, the amorphous phase of the STSe film is maintained up to 420 K, and the HEX phase appears at 560 K, which presents a significant improvement in phase change temperature. Unlike pure ST, however, there is a movement of the main peak position of STSe from 550 to 570 K, with the Raman shift variation from 119 to 188 and 251 cm^{-1} . These two vibration modes can be recognized into the heteropolar Sb–Se and nonpolar Sb–Sb vibration, respectively.⁴⁸ The result also indicates that Se was incorporated into Sb_2Te_3 and bonded with Sb. The contour map and the variations of normalized intensity are presented in Figure 4e,f. Since the bond energy of Sb–Se is relatively stronger than that of the Sb–Te bond and not easy to be destroyed, STSe presents a significant improvement in crystallization temperature and thermal stability. In general, compared with undoped ST, the crystallinity of the ST phase was suppressed with the phase change temperature increased about 60 K after the Se doping.

The effect of Se doping on the resistivity of ST is of much concern to the electrical performance of PCRAM; thus, the temperature-dependent resistance measurement (R – T) was performed and is illustrated in Figure 5a. As plotted in Figure 5c–e, the resistance of amorphous ST is relatively low ($\sim 10^5 \Omega$) and does not show an obvious abrupt drop, which may be attributed to a partial crystallization in the as-deposited state. For comparison, Figure 5b illustrates the temperature dependence of the resistance of commercialized GST. The resistance ON/OFF ratio value of GST exhibited 6 orders of magnitude, illustrating its application advantage in PCRAM. For the flat STSe film in Figure 5g, a sudden drop in resistance is displayed when the crystallization temperature is reached (~ 450 K), which can be ascribed to the amorphous to metastable FCC transformation. Moreover, with the increasing temperature, the resistance of STSe presents a slow and continuous decrease to a lower value (from 10^6 to $10^3 \Omega$) and reaches a stable value at 550 K, which is caused by the conversion from the metastable FCC to the HEX structure. The phase transformation temperatures obtained from resistance–temperature measurement were almost consistent with Raman results. In comparison with undoped ST, STSe demonstrates higher resistance in the amorphous state, which is beneficial to reduce the operation energy for RESET (amorphous state to crystalline state) operation.⁴⁹ In order to evaluate the thermal stability of flexible STSe devices, the R – T curves were also measured in the compression and tension strain state. A semicircular column mode of 4 mm radius was used to bend the flexible devices. As shown in Figure 5c,e for ST and Figure 5f,h for STSe, the flexible devices in compressive and tensile strain states displayed similar electrical behaviors compared with those in the flat state, including the phase change temperature and ON/OFF ratio in PCRAM. In general, these results confirm that the flexible STSe device is highly stable thermally and mechanically. According to Young-Chang Joo's theory,⁵⁰ the variation of stresses caused by the densities during the phase change process is approximately 170 MPa.⁵¹ For comparison, the compressive and tension stress caused by the bending test is insignificant. Furthermore, for the flexible STSe devices, the whole material and device were fabricated at

relatively low temperature (less than 600 K), which illustrated the potential compatibility in flexible electronic applications.

To achieve the device with much faster thermal response, the PCM layers were placed directly in contact with the heater. The metal–PCM–metal vertical sandwich structure phase change memory was fabricated, making the thermal resistance and thermal capacitance between the heater and the PCM layer much smaller. Figure 6 shows the device structure and

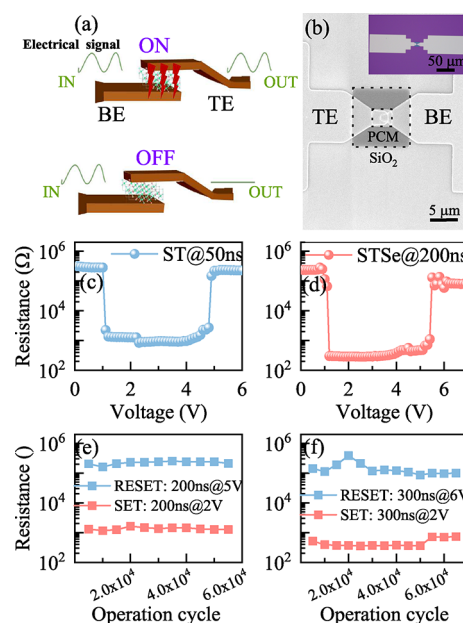


Figure 6. (a) Illustration of the electrical signal transmission and device structure of the PCRAM. (b) Zoomed-in plan-view SEM image of a PCRAM cell. The inset is a top-view optical image of a PCRAM. Cell resistances measured as a function of the voltage pulse for (c) ST- and (d) STSe-based PCRAM cells. Endurance characteristics of (e) ST- and (f) STSe-based PCRAM cells.

PCRAM cell performance based on ST and STSe. Figure 6a,b shows the 3D perspective and scanning electron microscopy (SEM) images of the PCRAM cell, respectively. As can be seen from Figure 6c, the SET and RESET operations for the ST test cell are achieved by a pulse amplitude of 1 and 4.8 V at a pulse length of 50 ns, respectively. Compared with the high-speed operation of ST-based PCRAM, a complete crystallization could be achieved with a SET voltage of 1.1 V and a RESET voltage of 5.4 V for re-amorphization for the STSe-based PCRAM cell at a 200 ns electric pulse. Note that the high SET and RESET voltage can be ascribed to the stronger Sb–Se bonds in c-STSe and reciprocity between Sb and Se in a-STSe, which is consistent with XPS and CDD results. It proves that the STSe test cell has the capability of high-stability operation. Figure 6e,f exhibits the endurance characteristics of ST-based and STSe-based phase change memory, with 200 ns@5 V RESET voltage and 200 ns@2 V SET voltage for ST-based PCRAM and 300 ns@6 V RESET voltage and 300 ns@2 V SET voltage for STSe-based PCRAM. ST shows a reversible switching up to 55 000 cycles, with STSe's up to 65 000 cycles. The relatively poor endurance of ST can be ascribed to the large density change during the phase transformation; further improvement in the endurance performance of the flexible PCRAM deserves a separate investigation in our future work. The cell resistance during the cycling process remains relatively stable, and the ON/OFF ratio is much more than 2 orders of

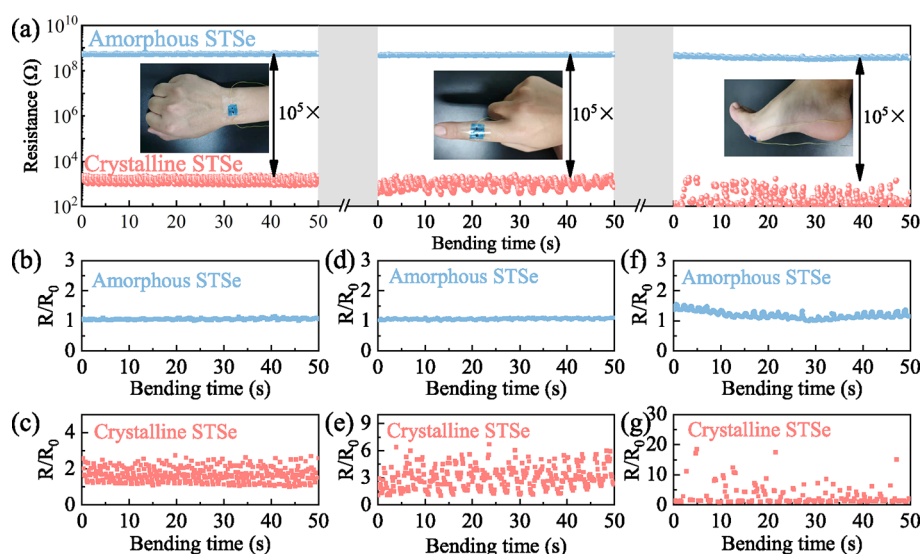


Figure 7. (a) Variations in resistance of the STSe devices as a function of the bending time. The insets exhibit the flexible STSe devices mounted on the wrist, finger, and foot. Time-dependent relative resistance change (R/R_0) responses of the a-STSe- and c-STSe-based flexible devices attached to the wrist (b,c), finger (d,e), and foot (f,g) when the subject was periodically changed.

magnitude, which can rival that of the YST-doped ST-based device,²⁶ indicating that STSe with suitable composition is a promising novel PCM.

Since the thermal stability of ST can be improved by Se incorporation due to the strong Sb–Se covalent bond, the mechanical performance and reliable operations of STSe phase change devices are worthy of further study. In consequence, we assembled flexible devices for sensing human activities in different parts of the body for wearable electronic potential application. The insets in Figure 7a exhibit the flexible STSe devices mounted on the cross-sectional body parts, like the wrist, finger, and foot, for the mechanical reliability evaluation. Real-time responses of the flexible electronics when applied with a tiny touch were investigated. The resistance waves exhibited a negligible change in resistance as the input tension waves under a dynamic strain with different body gestures' swing. In both circumstances, the resistances of the HRS and LRS were clearly distinguished, with a resistance ratio of over 10^5 , suggesting its potential for practical operations. More specifically, the resistance relative response R/R_0 of HRS and LRS devices upon a tiny touch with the wrist, finger, and foot at different times is depicted in Figure 7b–f, respectively. The relative resistance response of a-STSe was smaller than 1.5. As compared with a-STSe, c-STSe shows relatively larger R/R_0 within the range of 2–20. It should be pointed out that the difference in the R/R_0 value is due to differences in the speed and degree of body movement. Even after some repetitive stretching cycles, the response of the flexible devices remained outstandingly stable. The recoverability response clearly indicates that the STSe-based flexible electronics present a sensing function for practical application, which can suffer complex strain and still maintain its stability and excellent performance.

In real-world application, stable operations under dynamic and static behavior are crucial for wearable electrical devices. For further confirming the high dynamic mechanical stability, the electrical response of the amorphous and crystalline STSe devices was measured under a dynamic bending process on a self-made bending stage machine. The flexible device could be bent from a pristine flat status to an arcuation with a bending

radius of 2 mm, and the resistance of STSe sensing devices in amorphous and crystalline states was measured *in situ*. The time-dependent resistance in a dynamic bending process with a bias of 1 V can be demonstrated in Figure 8a. To make the

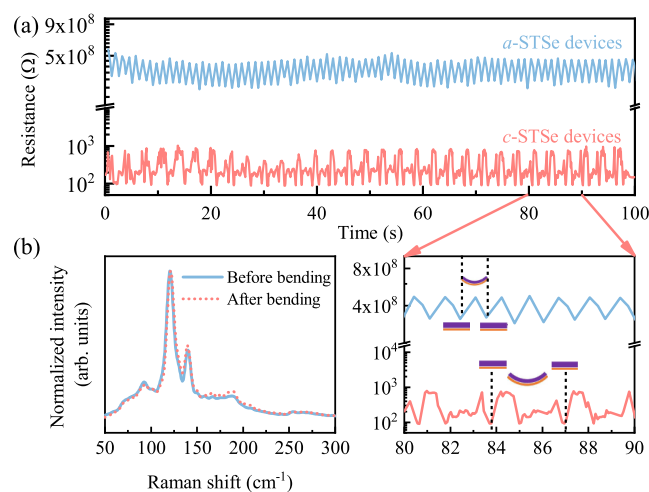


Figure 8. (a) Resistance of amorphous and crystalline STSe flexible devices vs time and the zoomed-in version in 80–90 s. (b) Raman spectra of STSe before and after bending for 100 s.

resistance variation more concrete, a zoomed-in version in 80–90 s is exhibited. The changes in resistance of a-STSe devices occurred periodically with time and are constrained within 3×10^8 to $5 \times 10^8 \Omega$ while those of the crystalline STSe devices are of 10^2 to $10^3 \Omega$. For a-STSe, in each cycle, as the flexible electronics bend from a flat state to a state of minimum curvature, the resistance increases in a non-linear and simple way. However, the c-STSe devices showed much complicated endurance under mechanically stressed conditions. With the STSe apparatus gradually bending, the resistance rapidly increases to a certain value and then decreases slightly. Furthermore, the resistance rises slightly and then gradually decreases when the stress is removed. The hysteresis phenomenon of c-STSe can be attributed to the grain

boundary scattering and vacancy in the crystal. On the whole, the resistance ratio between the amorphous state and the crystalline state values of the STSe was maintained without any significant change during the mechanical durability test, suggesting the good bending stability. In addition, the Raman spectra of STSe were also obtained to examine the film quality before and after the bending test, as shown in Figure 8b. The Raman spectra did not change after bending cycles, which indicates that the film quality is still preserved after bending for 100 s, exhibiting favorable endurance performance.

Long-term working reliability is an important factor to determine the feasibility in flexible memory application and wearable devices. Herein, we measured the endurance and retention of the STSe cell through different bending times at a fixed bending radius of 4 mm using a semicircular column mode in a probe station, as shown in Figure 9a. To

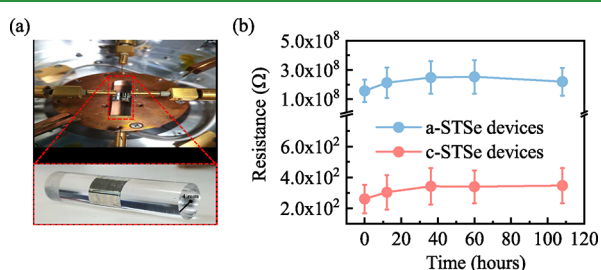


Figure 9. (a) Measurement setup for flexible devices under a bending radius of 4 mm. (b) Resistance variation of a-STSe- and c-STSe-based flexible devices as a function of the bending time. The device performance was averaged out with a set of nine cells.

demonstrate the repeatability and uniformity, nine different cells were fabricated and analyzed statistically. For any tested cell, the typical Ohmic contact of the STSe/top electrode was presented (Figure S8). As shown in Figure 9b, the resistance of amorphous STSe maintained $\sim 10^8 \Omega$ while that of the crystalline STSe sustained $\sim 10^2 \Omega$, even after static bending for more than 100 h. The resistance ON/OFF ratio value of the STSe maintains 6 orders of magnitude and remains nearly constant without any significant change during the durability test process, which also indicates that our flexible STSe devices are highly stable. Actually, the STSe film grown on the mica substrate is a growth mode similar to van der Waals epitaxy. Thus, there are no dangling bonds between layers, and the interlayer force in the phase change film is relatively small, which is beneficial for improving its stability.

To further quantify and understand the stress influence on the stability of the flexible STSe devices, the devices in various bending states should be carefully explored. The strain S induced on the surface of the flexible device by bending the substrate to a radius of R can be given by the following equation

$$S = \frac{(t_L + t_S)(1 + 2\eta + \chi\eta^2)}{2R(1 + \eta)(1 + \chi\eta)} \quad (1)$$

where $\eta = t_p/t_S$, $\chi = Y_p/Y_S$, t_p and t_S are the thickness of the PCM and the substrate, and Y_p and Y_S are the Young's modulus of the PCM and the substrate, respectively.^{52,53} Since the thickness of the PCM (~ 100 nm) is much less than that of the mica substrate ($\sim 20 \mu\text{m}$), S can be simply expressed as $t_p + t_S/2R$ (R is the bending radius).⁵⁴ By calculation, when the R is

reduced to 2 mm, the strain induced in the PCM layer is less than 0.5%, which is small enough to benefit the flexible STSe device working safely under the compressive and tension stress. In general, supported by the excellent flexibility of the mica substrate and the PCM layer, the STSe sensor is featured by ultrastability, good recognition, and the simple and facial fabrication process. The good performance achieved by STSe indicates the potential implementation in practical applications such as the medical industry, especially the electronic technology for point-of-care devices.^{55,56} Besides, the STSe-based sensing electronic skin could also provide real-time monitoring of muscle activity, which may be employed for useful clinic gait analysis and evaluate one's fatigue state.

4. CONCLUSIONS

In summary, we have investigated a reliable STSe PCM *via* doping engineering; the STSe-based PCRAM and highly functional flexible device were fabricated and assembled, which demonstrates appropriate thermal and mechanical ultra-stability. The incorporation of Se improved the thermal stability of Sb_2Te_3 with the phase change temperature from amorphous to FCC and HEX structures of 420 and 550 K, respectively. The results can be attributed to the stronger reciprocity between Sb and Se in a-STSe and stronger bonding energy of Sb–Se in c-STSe based on our CDD simulation results. Benefitting from this, STSe displayed a resistance ON/OFF ratio of 6 orders of magnitude even under compression or tension strain. The STSe-based phase change memory shows a relatively higher SET and RESET voltage than the ST-based cell and a reversible switching up to 65 000 cycles due to the improved stability. Moreover, the assembled flexible and wearable STSe device can realize the sensing of human activities, which demonstrates excellent recoverability and stability response. In addition, the favorable mechanical stability was verified through the bending fatigue test; the resistance of the amorphous and crystalline STSe was maintained without any significant change, suggesting the good mechanical durability and sustainability. The endurance and long-term operation reliability retention test with statistical analysis further confirmed the stability and reliability of the STSe device, including a large resistance ratio of over 10^6 and excellent endurance over 100 s and long retention over 100 h. The good flexibility and bendability of STSe electronic devices can be attributed to the small bending strain (less than 0.5%) induced to the PCM layer and the enhanced localization of Sb–Se bonds than that of Sb–Te bonds. Our work demonstrates that the ultra-stability of a Se-doped Sb_2Te_3 -based flexible PCM with favorable durability, sustainability, and good performance may open up their application opportunity for flexible chalcogenide-based memory devices and wearable device application.

■ ASSOCIATED CONTENT

Supporting Information

The Supporting Information is available free of charge at <https://pubs.acs.org/doi/10.1021/acsami.2c13792>.

Vertical sandwich structure phase change memory fabrication process flow, basic structure, composition, morphology, optics, and electricity properties of ST and STSe films including structure evolution and surface topographies at varied annealing temperature, HRTEM and elemental composition, transmittance spectrum and

the calculated E_g of STSe membranes, typical Ohmic contact curves of top electrode/STSe, and comparison table of this work with other flexible phase change memory devices (PDF)

AUTHOR INFORMATION

Corresponding Authors

Anyang Cui – Technical Center for Multifunctional Magneto-Optical Spectroscopy (Shanghai), Engineering Research Center of Nanophotonics & Advanced Instrument (Ministry of Education), Department of Physics, School of Physics and Electronic Science, East China Normal University, Shanghai 200241, China; Email: aycui@phy.ecnu.edu.cn

Zhigao Hu – Technical Center for Multifunctional Magneto-Optical Spectroscopy (Shanghai), Engineering Research Center of Nanophotonics & Advanced Instrument (Ministry of Education), Department of Physics, School of Physics and Electronic Science, East China Normal University, Shanghai 200241, China; Collaborative Innovation Center of Extreme Optics, Shanxi University, Taiyuan 030006, China; Shanghai Institute of Intelligent Electronics & Systems, Fudan University, Shanghai 200433, China; orcid.org/0000-0003-0575-2191; Phone: +86-21-54345150; Email: zghu@ee.ecnu.edu.cn; Fax: +86-21-54342933

Authors

Shubing Li – Technical Center for Multifunctional Magneto-Optical Spectroscopy (Shanghai), Engineering Research Center of Nanophotonics & Advanced Instrument (Ministry of Education), Department of Physics, School of Physics and Electronic Science, East China Normal University, Shanghai 200241, China

Ming Li – Technical Center for Multifunctional Magneto-Optical Spectroscopy (Shanghai), Engineering Research Center of Nanophotonics & Advanced Instrument (Ministry of Education), Department of Physics, School of Physics and Electronic Science, East China Normal University, Shanghai 200241, China

Li Chen – Technical Center for Multifunctional Magneto-Optical Spectroscopy (Shanghai), Engineering Research Center of Nanophotonics & Advanced Instrument (Ministry of Education), Department of Physics, School of Physics and Electronic Science, East China Normal University, Shanghai 200241, China

Xionghu Xu – Technical Center for Multifunctional Magneto-Optical Spectroscopy (Shanghai), Engineering Research Center of Nanophotonics & Advanced Instrument (Ministry of Education), Department of Physics, School of Physics and Electronic Science, East China Normal University, Shanghai 200241, China

Xin Zhou – Technical Center for Multifunctional Magneto-Optical Spectroscopy (Shanghai), Engineering Research Center of Nanophotonics & Advanced Instrument (Ministry of Education), Department of Physics, School of Physics and Electronic Science, East China Normal University, Shanghai 200241, China

Kai Jiang – Technical Center for Multifunctional Magneto-Optical Spectroscopy (Shanghai), Engineering Research Center of Nanophotonics & Advanced Instrument (Ministry of Education), Department of Physics, School of Physics and Electronic Science, East China Normal University, Shanghai 200241, China

Liyan Shang – Technical Center for Multifunctional Magneto-Optical Spectroscopy (Shanghai), Engineering Research Center of Nanophotonics & Advanced Instrument (Ministry of Education), Department of Physics, School of Physics and Electronic Science, East China Normal University, Shanghai 200241, China; orcid.org/0000-0003-2341-3978

Yawei Li – Technical Center for Multifunctional Magneto-Optical Spectroscopy (Shanghai), Engineering Research Center of Nanophotonics & Advanced Instrument (Ministry of Education), Department of Physics, School of Physics and Electronic Science, East China Normal University, Shanghai 200241, China; orcid.org/0000-0001-8776-5687

Jinzhong Zhang – Technical Center for Multifunctional Magneto-Optical Spectroscopy (Shanghai), Engineering Research Center of Nanophotonics & Advanced Instrument (Ministry of Education), Department of Physics, School of Physics and Electronic Science, East China Normal University, Shanghai 200241, China; orcid.org/0000-0003-1511-4281

Liangqing Zhu – Technical Center for Multifunctional Magneto-Optical Spectroscopy (Shanghai), Engineering Research Center of Nanophotonics & Advanced Instrument (Ministry of Education), Department of Physics, School of Physics and Electronic Science, East China Normal University, Shanghai 200241, China

Junhao Chu – Technical Center for Multifunctional Magneto-Optical Spectroscopy (Shanghai), Engineering Research Center of Nanophotonics & Advanced Instrument (Ministry of Education), Department of Physics, School of Physics and Electronic Science, East China Normal University, Shanghai 200241, China; Collaborative Innovation Center of Extreme Optics, Shanxi University, Taiyuan 030006, China; Shanghai Institute of Intelligent Electronics & Systems, Fudan University, Shanghai 200433, China

Complete contact information is available at: <https://pubs.acs.org/10.1021/acsami.2c13792>

Author Contributions

The manuscript was written through contributions of all authors. All authors have given approval to the final version of the manuscript.

Notes

The authors declare no competing financial interest.

ACKNOWLEDGMENTS

This work was financially supported by the National Natural Science Foundation of China (grant no. 62090013), the National Key Research and Development Program of China (grant no. 2019YFB2203403), the National Natural Science Foundation of China (grant nos. 61974043, 62074058, 12104156, 61974044, and 91833303), the Projects of Science and Technology Commission of Shanghai Municipality (grant nos. 21JC1402100 and 19511120100), the China Postdoctoral Science Foundation (grant nos. 2020TQ0099 and 2020M681222), the Program for Professor of Special Appointment (Eastern Scholar) at Shanghai Institutions of Higher Learning, and Shanghai Pujiang Program (20PJ1403600).

REFERENCES

- (1) Gu, M.; Zhang, Q. M.; Lamon, S. Nanomaterials for Optical Data Storage. *Nat. Rev. Mater.* **2016**, *1*, 16070.

- (2) Cao, Q.; Lü, W. M.; Wang, R.; Guan, X. W.; Wang, L.; Yan, S. S.; Wu, T.; Wang, X. L. Nonvolatile Multistates Memories for High-Density Data Storage. *ACS Appl. Mater. Interfaces* **2020**, *12*, 42449–42471.
- (3) Ovshinsky, S. R. Reversible Electrical Switching Phenomena in Disordered Structures. *Phys. Rev. Lett.* **1968**, *21*, 1450–1453.
- (4) Lencer, D.; Salinga, M.; Grabowski, B.; Hickel, T.; Neugebauer, J.; Wuttig, M. A Map for Phase-Change Materials. *Nat. Mater.* **2008**, *7*, 972–977.
- (5) Zhang, W.; Mazzarello, R.; Wuttig, M.; Ma, E. Designing Crystallization in Phase-Change Materials for Universal Memory and Neuro-Inspired Computing. *Nat. Rev. Mater.* **2019**, *4*, 150–168.
- (6) Wang, X.; Cui, A. Y.; Chen, F. F.; Xu, L. P.; Hu, Z. G.; Jiang, K.; Shang, L. Y.; Chu, J. H. Probing Effective Out-of-Plane Piezoelectricity in van der Waals Layered Materials Induced by Flexoelectricity. *Small* **2019**, *15*, 1903106.
- (7) Liu, B.; Li, K. Q.; Liu, W. L.; Zhou, J.; Wu, L. C.; Song, Z. T.; Elliott, S. R.; Sun, Z. M. Multi-Level Phase-Change Memory with Ultralow Power Consumption and Resistance Drift. *Sci. Bull.* **2021**, *66*, 2217–2224.
- (8) Lu, Y. M.; Li, X.; Yan, B. N.; Yan, L. H.; Zhang, T.; Song, Z. T.; Huang, R.; Yang, Y. C. In-Memory Realization of Eligibility Traces Based on Conductance Drift of Phase Change Memory for Energy-Efficient Reinforcement Learning. *Adv. Mater.* **2022**, *34*, 2107811.
- (9) Shen, J. B.; Jia, S. J.; Shi, N. N.; Ge, Q. Q.; Gotoh, T.; Lv, S. L.; Liu, Q.; Dronskowski, R.; Elliott, S. R.; Song, Z. T.; Zhu, M. Elemental Electrical Switch Enabling Phase Segregation-Free Operation. *Science* **2021**, *374*, 1390–1394.
- (10) Kim, I. S.; Cho, S. L.; Im, D. H.; Cho, E. H.; Kim, D. H.; Oh, G. H.; Ahn, D. H.; Park, S. O.; Nam, S. W.; Moon, J. T.; Chung, C. H. High Performance PRAM Cell Scalable to Sub-20 nm Technology with below $4F^2$ Cell Size, Extendable to DRAM Applications. Symposium on VLSI Technology, 2010; pp 203–204.
- (11) Hu, Y. F.; Zou, H.; Yuan, L.; Xue, J. Z.; Sui, Y. X.; Wu, W. H.; Zhang, J. H.; Zhu, X. Q.; Song, S. N.; Song, Z. T. Improved Phase Change Behavior of Sb₂Se Material by Si Addition for Phase Change Memory. *Scr. Mater.* **2016**, *115*, 19–23.
- (12) Xia, M. J.; Zhu, M.; Wang, Y. C.; Song, Z. T.; Rao, F.; Wu, L. C.; Cheng, Y.; Song, S. N. Ti-Sb-Te Alloy: A Candidate for Fast and Long-Life Phase-Change Memory. *ACS Appl. Mater. Interfaces* **2015**, *7*, 7627–7634.
- (13) Wang, G. X.; Chen, Y. M.; Shen, X.; Li, J. J.; Wang, R. P.; Lu, Y. G.; Dai, S. X.; Xu, T. F.; Nie, Q. H. Reversibility and Stability of ZnO-Sb₂Te₃ Nanocomposite Films for Phase Change Memory Applications. *ACS Appl. Mater. Interfaces* **2014**, *6*, 8488–8496.
- (14) Khan, A. I.; Daus, A.; Islam, R.; Neilson, K. M.; Lee, H. R.; Wong, H.-S. P.; Pop, E. Ultralow-Switching Current Density Multilevel Phase-Change Memory on a Flexible Substrate. *Science* **2021**, *373*, 1243–1247.
- (15) Kim, D. H.; Lee, H. E.; You, B. K.; Cho, S. B.; Mishra, R.; Kang, I.-S.; Lee, K. J. Flexible Crossbar-Structured Phase Change Memory Array via Mo-based Interfacial Physical Lift-off. *Adv. Funct. Mater.* **2018**, *29*, 1806338.
- (16) Wang, J. N.; Xiong, B.; Peng, R. W.; Li, C. Y.; Hou, B. Q.; Chen, C. W.; Liu, Y.; Wang, M. Flexible Phase Change Materials for Electrically-Tuned Active Absorbers. *Small* **2021**, *17*, 2101282.
- (17) Mun, B. H.; You, B. K.; Yang, S. R.; Yoo, H. G.; Kim, J. M.; Park, W. I.; Yin, Y.; Byun, M.; Jung, Y. S.; Lee, K. J. Flexible One Diode-One Phase Change Memory Array Enabled by Block Copolymer Self-Assembly. *ACS Nano* **2015**, *9*, 4120–4128.
- (18) Kao, K. F.; Lee, C. M.; Chen, M. J.; Tsai, M. J.; Chin, T. S. Ga₂Te₃Sb₅-A Candidate for Fast and Ultralong Retention Phase-Change Memory. *Adv. Mater.* **2009**, *21*, 1695–1699.
- (19) Rao, F.; Ding, K. Y.; Zhou, Y. X.; Zheng, Y. H.; Xia, M. J.; Lv, S. L.; Song, Z. T.; Feng, S. L.; Ronneberger, I.; Mazzarello, R.; Zhang, W.; Ma, E. Reducing the Stochasticity of Crystal Nucleation to Enable Subnanosecond Memory Writing. *Science* **2017**, *358*, 1423–1427.
- (20) Zhao, J.; Song, W. X.; Xin, T. J.; Song, Z. T. Rules of Hierarchical Melt and Coordinate Bond to Design Crystallization in Doped Phase Change Materials. *Nat. Commun.* **2021**, *12*, 6473.
- (21) Zhang, X.; Zhang, Z. H.; Song, S. N.; Zheng, Q. Q.; Yu, W. L.; Zheng, W. T.; Zhu, X. W.; Shao, H. H.; Zhang, J.; Chen, L. L. Characterization of Ge Ions Implantation in Sb₂Te₃ Thin Films for High Speed Phase Change Memory Application. *Appl. Phys. Lett.* **2019**, *115*, 103105.
- (22) Yin, Y.; Sone, H.; Hosaka, S. Characterization of Nitrogen Doped Films and Their Application to Phase-Change Memory. *J. Appl. Phys.* **2007**, *102*, 064503.
- (23) Zhu, M.; Wu, L. C.; Rao, R.; Song, Z. T.; Ren, K.; Ji, X. L.; Song, S. N.; Yao, D. N.; Feng, S. L. Uniform Ti-doped Sb₂Te₃ Materials for High-Speed Phase Change Memory Applications. *Appl. Phys. Lett.* **2014**, *104*, 053119.
- (24) Shen, J. B.; Lv, S. L.; Chen, X.; Li, T.; Zhang, S. F.; Song, Z. T.; Zhu, M. Thermal Barrier Phase Change Memory. *ACS Appl. Mater. Interfaces* **2019**, *11*, 5336–5343.
- (25) Zhu, M.; Xia, M. J.; Rao, F.; Li, X. B.; Wu, L. C.; Ji, X. L.; Lv, S. L.; Song, Z. T.; Feng, S. L.; Sun, H. B.; Zhang, B. S. One Order of Magnitude Faster Phase Change at Reduced Power in Ti-Sb-Te. *Nat. Commun.* **2014**, *5*, 4086.
- (26) Liu, B.; Liu, W. L.; Li, Z.; Li, K. Q.; Wu, L. C.; Zhou, J.; Song, Z. T.; Sun, Z. M. Y-Doped Sb₂Te₃ Phase-Change Materials: Toward a Universal Memory. *ACS Appl. Mater. Interfaces* **2020**, *12*, 20672–20679.
- (27) Zhu, M.; Song, W. X.; Konze, P. M.; Li, T.; Gault, B.; Chen, X.; Shen, J. B.; Lv, S. L.; Song, Z. T.; Wuttig, M.; Dronskowski, R. Direct Atomic Insight into the Role of Dopants in Phase-Change Materials. *Nat. Commun.* **2019**, *10*, 3525.
- (28) Li, X. L.; Sun, Z. M.; Song, Z. T.; Rao, F.; Wu, L. C.; Liu, W. L. *Ab Initio* Study of Sb₂Se_xTe_{3-x} ($x=0, 1, 2$) Phase Change Materials. *Solid State Sci.* **2011**, *13*, 131–134.
- (29) Yin, Y.; Morioka, S.; Kozaki, S.; Satoh, R.; Hosaka, S. Oxygen-Doped Sb₂Te₃ for High-Performance Phase-change Memory. *Appl. Surf. Sci.* **2015**, *349*, 230–234.
- (30) Delaney, M.; Zeimpekis, I.; Lawson, D.; Hewak, D. W.; Muskens, O. A New Family of Ultralow Loss Reversible Phase Change Materials for Photonic Integrated Circuits: Sb₂S₃ and Sb₂Se₃. *Adv. Funct. Mater.* **2020**, *30*, 2002447.
- (31) Chen, L. L.; Song, S. N.; Song, Z. T.; Li, L.; Zhang, Z. H.; Zheng, Y. H.; Zheng, Q. Q.; Zhang, X.; Zhu, X. W.; Shao, H. H. Sb₅₂Se₃₆Te₁₂ Material with High-Temperature Data Retention Coupled with Rapid Crystallization Speed for Phase Change Application. *Appl. Surf. Sci.* **2015**, *357*, 603–607.
- (32) Tomelleri, M.; Hippert, F.; Lawson, D.; Farjot, T.; Licitra, C.; Vaxelaire, N.; Dory, J. B.; Benoit, D.; Giordano, V.; Noe, P. Overcoming the Thermal Stability Limit of Chalcogenide Phase-Change Materials for High-Temperature Applications in GeSe_{1-x}Te_x Thin Films. *Phys. Status Solidi RRL* **2021**, *15*, 2000451.
- (33) Zhang, Y. F.; Fowler, C.; Liang, J. H.; Azhar, B.; Shalaginov, M. Y.; Deckoff-Jones, S.; An, S. S.; Chou, J. B.; Roberts, C. M.; Liberman, V.; Kang, M.; Ros, C.; Richardson, K. A.; Rivero-Baleine, C.; Gu, T.; Zhang, H. L.; Hu, J. J. Electrically Reconfigurable Non-Volatile Metasurface using Low-Loss Optical Phase-Change Material. *Nat. Nanotechnol.* **2021**, *16*, 661–666.
- (34) Zhang, Y. F.; Chou, J. B.; Li, J. Y.; Li, H. S.; Du, Q. Y.; Yadav, A.; Zhou, Si.; Shalaginov, M. Y.; Fang, Z. R.; Zhong, H. K.; Roberts, C.; Robinson, P.; Bohlin, B.; Ríos, C.; Lin, H. T.; Kang, M.; Gu, T.; Warner, J.; Liberman, V.; Richardson, K.; Hu, J. J. Broadband Transparent Optical Phase Change Materials for High-Performance Nonvolatile Photonics. *Nat. Commun.* **2019**, *10*, 4279.
- (35) Yue, F. Y.; Piccoli, R.; Shalaginov, M. Y.; Gu, T.; Richardson, K. A.; Morandotti, R.; Hu, J. J.; Razzari, L. Nonlinear Mid-Infrared Metasurface based on a Phase-Change Material. *Laser Photonics Rev.* **2021**, *15*, 2000373.
- (36) Zhu, D. F.; Wang, X. Y.; Li, J.; Ye, H.; Yu, Z. Y.; Liu, Y. M. Design of Nonvolatile and Efficient Polarization-Rotating Optical

Switch with Phase Change Material. *Opt. Laser Technol.* **2022**, *151*, 108065.

(37) Li, Z.; Si, C.; Zhou, J.; Xu, H. B.; Sun, Z. M. Yttrium-Doped Sb_2Te_3 : A Promising Material for Phase-Change Memory. *ACS Appl. Mater. Interfaces* **2016**, *8*, 26126–26134.

(38) Hilmi, I.; Lotnyk, A.; Gerlach, J. W.; Schumacher, P.; Rauschenbach, B. Research Update: Van-der-Waals Epitaxy of Layered Chalcogenide Sb_2Te_3 Thin Films Grown by Pulsed Laser Deposition. *APL Mater.* **2017**, *5*, 050701.

(39) Kanagaraj, M.; Pawbake, A.; Sarma, C. S.; Rajaji, V.; Narayana, C.; Measson, M. A.; Peter, S. C. Structural, Magnetotransport and Hall Coefficient Studies in Ternary $\text{Bi}_2\text{Te}_2\text{Se}$, $\text{Sb}_2\text{Te}_2\text{Se}$ and $\text{Bi}_2\text{Te}_2\text{S}$ Tetradymite Topological Insulating Compounds. *J. Alloys Compd.* **2019**, *794*, 195–202.

(40) Zhu, M.; Wu, L. C.; Rao, F.; Song, Z. T.; Peng, C.; Li, X. L.; Yao, D. N.; Xi, W.; Feng, S. L. Phase Change Characteristics of SiO_2 Doped Sb_2Te_3 Materials for Phase Change Memory Application. *Electrochem. Solid-State Lett.* **2011**, *14*, H404–H407.

(41) Li, M.; Xie, M. Z.; Ji, H.; Zhou, J. Y.; Jiang, K.; Shang, L. Y.; Li, Y. W.; Hu, Z. G.; Chu, J. H. PLD-Derived $\text{Ge}_2\text{Sb}_2\text{Te}_5$ Phase-Change Films with Extreme Bending Stability for Flexible Device Applications. *Appl. Phys. Lett.* **2020**, *116*, 162102.

(42) Vinod, E. M.; Singh, A. K.; Ganesan, R.; Sangunni, K. S. Effect of Selenium Addition on the GeTe Phase Change Memory Alloys. *J. Alloys Compd.* **2012**, *537*, 127–132.

(43) Mann, J. B.; Meek, T. L.; Allen, L. C. Configuration Energies of the Main Group Elements. *J. Am. Chem. Soc.* **2000**, *122*, 2780–2783.

(44) Zhou, J.; Sun, Z. M.; Pan, Y.; Song, Z. T.; Ahuja, R. Vacancy or not: An Insight on the Intrinsic Vacancies in Rocksalt-Structured GeSbTe Alloys from *ab Initio* Calculations. *Europhys. Lett.* **2011**, *95*, 27002.

(45) Zhang, H. Y.; Cheng, Y.; Tang, M.; Chen, X. R.; Ji, G. F. First-Principles Study of Structural, Elastic, Electronic and Thermodynamic Properties of Topological Insulator Sb_2Te_3 under Pressure. *Comput. Mater. Sci.* **2015**, *96*, 342–347.

(46) Singh, M. P.; Mandal, M.; Sethupathi, K.; Rao, M. S. R.; Nayak, P. K. Study of Thermometry in Two-dimensional Sb_2Te_3 from Temperature-Dependent Raman Spectroscopy. *Nanoscale Res. Lett.* **2021**, *16*, 22.

(47) Hwang, S.; Park, H.; Kim, D.; Lim, H.; Lee, C.; Han, J. H.; Kwon, Y.-K.; Cho, M. H. Ultra-low Energy Phase Change Memory with Improved Thermal Stability by Tailoring the Local Structure through Ag Doping. *ACS Appl. Mater. Interfaces* **2020**, *12*, 37285.

(48) Zhou, Y.; Leng, M. Y.; Xia, Z.; Zhong, J.; Song, H. B.; Liu, X. S.; Yang, B.; Zhang, J. P.; Chen, J.; Zhou, K. H.; Han, J. B.; Cheng, Y. B.; Tang, J. Solution-processed Antimony Selenide Heterojunction Solar Cells. *Adv. Energy Mater.* **2014**, *4*, 1301846.

(49) Hilmi, I.; Lotnyk, A.; Gerlach, J. W.; Schumacher, P.; Rauschenbach, B. Research Update: Van-der-Waals Epitaxy of Layered Chalcogenide Sb_2Te_3 Thin Films Grown by Pulsed Laser Deposition. *APL Mater.* **2017**, *5*, 050701.

(50) Kolobov, A. V.; Mishchenko, A. S.; Fons, P.; Yakubenya, S. M.; Tominaga, J. A Possible Mechanism of Ultrafast Amorphization in Phase-change Memory Alloys: an Ion Slingshot from the Crystalline to Amorphous Position. *J. Phys.: Condens. Matter* **2007**, *19*, 455209.

(51) Park, I.-M.; Jung, J.-K.; Ryu, S.-O.; Choi, K.-J.; Yu, B.-G.; Park, Y.-B.; Han, S. M.; Joo, Y.-C. Thermomechanical Properties and Mechanical Stresses of $\text{Ge}_2\text{Sb}_2\text{Te}_5$ Films in Phase-change Random Access Memory. *Thin Solid Films* **2008**, *517*, 848–852.

(52) Suo, Z.; Ma, E. Y.; Gleskova, H.; Wagner, S. Mechanics of Rollable and Foldable Film-on-Foil Electronics. *Appl. Phys. Lett.* **1999**, *74*, 1177.

(53) Gleskova, H.; Wagner, S.; Suo, Z. Failure Resistance of Amorphous Silicon Transistors under Extreme in-plane Strain. *Appl. Phys. Lett.* **1999**, *75*, 3011.

(54) Zhou, Y.; Han, S. T.; Xu, Z. X.; Yang, X. B.; Ng, H. P.; Huang, L. B.; Roy, V. A. L. Functional High- k Nanocomposite Dielectrics for Flexible Transistors and Inverters with Excellent Mechanical Properties. *J. Mater. Chem.* **2012**, *22*, 14246.

(55) Lee, G.-H.; Moon, H.; Kim, H.; Lee, G. H.; Kwon, W.; Yoo, S.; Myung, D.; Yun, S. H.; Bao, Z. N.; Hahn, S. K. Multifunctional Materials for Implantable and Wearable Photonic Healthcare Devices. *Nat. Rev. Mater.* **2020**, *5*, 149–165.

(56) Lee, H. W.; Kim, E.; Lee, Y.; Kim, H.; Lee, J.; Kim, M.; Yoo, H.-J.; Yoo, S. Toward All-Day Wearable Health Monitoring: An Ultralow-Power, Reflective Organic Pulse Oximetry Sensing Patch. *Sci. Adv.* **2018**, *4*, No. eaas9530.